Materials Today Communications 54 (2026) 115701

Contents lists available at ScienceDirect

Materials Today Communications

journal homepage: www.elsevier.com/locate/mtcomm

Porosity and elevated-temperature tensile response of PBF-LB/M Ti-6Al-4V across laser beam profiles mapped using a spot-size-aware energy metric

Abid Ullah [a,b,*], Amjad Iqbal [c], Kai Zhang [d], Tingting Liu [d], Dirk Herzog [a,e], Alexander E. Medvedev [b], Andrey Molotnikov [b], Ingomar Kelbassa [a,e], Milan Brandt [b,**]

[a] Institute for Industrialization of Smart Materials, Hamburg University of Technology, Hamburg D-21079, Germany
[b] RMIT Centre for Additive Manufacturing, School of Engineering, RMIT University, Melbourne, VIC 3000, Australia
[c] School of Materials Science and Engineering, Nanjing University of Science and Technology, Nanjing 210094, China
[d] School of Mechanical Engineering, Nanjing University of Science and Technology, Nanjing 210094, China
[e] Fraunhofer Research Institution for Additive Manufacturing Technologies IAPT, Hamburg D-21029, Germany

A R T I C L E I N F O

Keywords:
Additive manufacturing
PBF-LB/M
Laser beam shaping
Relative density
High-temperature tensile properties
Ti-6Al-4V

A B S T R A C T

Laser beam shaping in PBF-LB/M modifies the spatial laser energy distribution, affecting melt-pool evolution, defect formation, and mechanical response. Ti-6Al-4V was processed using Gaussian, core–ring, and ring-dominated beam profiles. Measured beam maps were used to determine the effective beam diameter in a modified energy metric (VED_M, J mm^{-2} s^{-1}/^{2}) for cross-mode comparison. Densification and pore characteristics were assessed in cubes and tensile specimens. Core–ring and ring-dominated profiles transitioned from lack-of-fusion defects at low input to near-full density at higher input, whereas Gaussian shifted toward keyhole-type porosity at the highest input. At VED_M = 332 J mm^{-2} s^{-1} /^{2}, the μCT-scanned tensile gauge regions showed lower relative density for Gaussian (~98.6%) than for core–ring and ring-dominated conditions (~99.8%). Tensile specimens produced with Gaussian and ring-dominated beams were tested at RT, 200 °C, and 400 °C. All conditions showed temperature-dependent softening. However, at high VED_M and 400 °C, the ring-dominated condition retained higher ductility (~10%) than the Gaussian condition (~7%), while maintaining a comparable peak stress. Fractography showed pore-assisted initiation in the Gaussian condition and ductile tearing with pronounced necking in the ring-dominated condition. Overall, elevated-temperature tensile performance was primarily associated with pore type and severity, while VED_M provides a practical framework for cross-mode comparison.

1. Introduction

Laser powder bed fusion of metals (PBF-LB/M) produces near-net-shape parts by selectively melting powder layers with a focused laser beam, enabling complex geometries and refined microstructures that can contribute to high strength, while ductility and fatigue resistance remain highly sensitive to defects and processing conditions [1–3]. However, achieving consistent part quality remains challenging because the melt pool can become unstable, leading to defects such as porosity, cracking, and variable surface finish [4–6]. In most commercial systems, the laser intensity distribution is close to Gaussian, and its peaked irradiance can promote steep temperature gradients, evaporation and spatter, and keyhole instabilities when energy input is high, while insufficient energy and overlap can result in lack-of-fusion voids and unmelted regions [7,8]. These defect types are mechanically critical since they act as stress concentrators and common crack-initiation sites, reducing ductility and fatigue resistance [9], and they typically make the processing window highly sensitive to parameter changes and geometry effects [10,11].

Beam shaping has attracted increasing attention as a process-level lever to tailor the spatial distribution of laser power in PBF-LB/M and thereby influence melt-pool stability, defect formation, and the usable processing window [12,13]. By moving beyond a conventional Gaussian spot, the energy delivery can be adjusted without changing the overall process concept, encouraging work on non-Gaussian profiles and their effect on build quality and performance [14,15]. Much of the current

* Corresponding author at: Institute for Industrialization of Smart Materials, Hamburg University of Technology, Hamburg D-21079, Germany.
** Corresponding author.
E-mail addresses: abid.ullah@tuhh.de, abidmech95@gmail.com (A. Ullah), milan.brandt@rmit.edu.au (M. Brandt).

https://doi.org/10.1016/j.mtcomm.2026.115701
Received 1 May 2026; Received in revised form 3 June 2026; Accepted 9 July 2026
Available online 9 July 2026
2352-4928/

beam-shaping literature focuses on changes in track formation, melt-pool behavior [16,17], build density [18], and process-window expansion, while fewer studies extend the discussion to microstructure and mechanical properties. Bayat et al. [19] combined numerical and experimental work to explore spatial beam shaping in PBF-LB/M of Ti6Al4V and its potential for controlling melt-pool conditions and enabling tailored properties. Pérez-Ruiz et al. [20] compared Gaussian and ring beams for PBF-LB/M IN718 and reported clear differences in densification, melt-pool characteristics, and mechanical properties. Godec et al. [21] showed that switching from Gaussian to ring-shaped beams can alter the as-built microstructure and build-direction sensitivity, and that optimized post-heat treatment is needed to recover comparable tensile properties in nickel-based alloy IN718. At the same time, Chechik et al. [22] showed that the influence of ring/spot profiles is material dependent, cautioning against generalizing "ring-beam benefits" across alloys without systematic validation. For Ti-6Al-4V, Wang et al. [23] demonstrated high-density fabrication using a flat-top beam and examined how processing parameters affect microstructure and resulting physical properties. Collectively, these studies show that modifying the laser energy distribution can widen the process window and alter defect evolution across lack-of-fusion, stable conduction, and keyhole-related regimes. However, it remains unclear whether beam-shape-dependent pore populations translate into measurable differences in tensile response under service-relevant conditions. This question is particularly important for Ti-6Al-4V, where mechanical reliability is highly sensitive not only to porosity level, but also to pore type, size, and spatial distribution [24,25]. Moreover, most beam-shaping studies assess performance primarily at room temperature, although elevated temperature can change plastic flow, damage evolution, and defect sensitivity [26,27]. As a result, studies that directly combine quantitative pore characterization, tensile testing at room and elevated temperatures, and fracture-surface analysis across different beam shapes remain scarce.

This study investigates porosity formation and elevated-temperature tensile response of PBF-LB/M Ti-6Al-4V across three laser beam profiles: Gaussian, core–ring, and ring-dominated. Tensile testing was conducted for the Gaussian and ring-dominated profiles, representing the two end-member energy distributions. A practical, modified, and normalized energy metric is used to select comparable processing conditions across modes. Porosity and densification are evaluated across a low-to-high energy input range to distinguish lack-of-fusion from keyhole-type porosity. Finally, fracture-surface microscopy is employed to relate the tensile response to the dominant damage initiation sites and fracture mechanisms.

2. Experimental design

2.1. Materials and PBF-LB/M processing

All specimens were produced from gas-atomized Ti-6Al-4V Grade 5 powder (Höganäs Germany GmbH, Goslar, Germany) with a nominal particle size range of 15–53 μm. SEM images of the initial Ti-6Al-4V powder show predominantly spherical particles with occasional satellites/irregular particles (Supplementary Fig. S1). No obvious surface-open pores were observed. Specimens were fabricated on an AMCM M290–2 FLX system equipped with an nLIGHT AFX laser−1000 (nLIGHT, Inc., Camas, WA, USA) beam-shaping module. Two geometries were manufactured: (i) cubes (10 × 10 × 10 mm^3) for densification/porosity assessment and microscopy, and (ii) cylindrical rods (92 mm × Ø8 mm). The rods were initially produced for conventional room-temperature tensile testing. However, after the scope was extended to elevated-temperature testing, miniature flat specimens were machined from the rods to meet the requirements of the high-temperature test setup. This approach preserved a common build history across all tensile conditions and provided a consistent final geometry and surface preparation route for the miniature tensile specimens. A bidirectional meander hatch was used with a hatch angle of 45° relative to the build-plane x-axis, rotated by 90° between successive layers, following EN ISO/ASTM 52921:2016. Beam intensity distributions were measured up to 200 W using a CCD beam profiler (SP928, Ophir Spiricon Europe GmbH, Germany). The beam was attenuated using an LBS−300 beam splitter (≈0.01% transmission to the sensor) and two neutral-density filters providing a total attenuation of ND4.

2.2. Process parameters and energy metrics

Three laser beam profiles were investigated: M0 (Gaussian), M3 (core–ring mode), and M6 (ring-dominated mode). For each profile, laser power P, scan speed v, and hatch spacing h were varied. The corresponding parameter sets are summarized in Tables 1 and 2. For reference and comparability with conventional PBF-LB/M literature, the classical volumetric energy density is defined as

$$VED = \frac{P}{vht} \tag{1}$$

where P is laser power, v speed, h hatch spacing, and t layer thickness. Since VED does not account for laser–material interaction time or the effective beam size, it is not fully sufficient for comparing different beam intensity distributions [28]. To provide the basis for the spot-size-aware energy metric used in this work, the Ferro-based effective energy-density scaling [29], is briefly recalled as:

$$E_{d,\mathrm{eff}} = \frac{\beta}{h\sqrt{4\alpha\Phi}}\frac{P}{\sqrt{v}} \tag{2}$$

where Φ is the effective beam diameter at the build plane, $\alpha = k/(\rho C_p)$ is the thermal diffusivity (k thermal conductivity, ρdensity, $C_p$heat capacity), and $\beta$is an effective absorptivity factor. A similar approach is also suggested by Wischeropp et al. [12].

Because β is not directly measured and may vary with processing conditions, we additionally report a normalized spot-size-aware parameter obtained from $E_{d,\mathrm{eff}}$ by omitting the material/absorptivity prefactor:

$$VED_M \equiv E^* = \frac{P}{h\sqrt{v\,\Phi}}. \tag{3}$$

In this study, $\mathrm{VED_M}$ ($\mathrm{J\,mm^{-2}\,s^{-1/2}}$) is used to support consistent relative comparison across beam shapes. Throughout this work, Φ is taken as the measured build-plane effective beam diameter $D_{0.1,\mathrm{eq}}$, defined as the equivalent diameter at the 10% $I_{\max}$ contour extracted from the 2D beam maps. Consistent with recent energy-scaling and process-window studies, $\mathrm{VED_M}$ is used here as a spot-size-aware comparative descriptor to organize low, intermediate, and high-input regimes across beam modes, rather than as a universal melt-pool stability criterion. Therefore, the $\mathrm{VED_M}$ based trends are interpreted together with the measured beam profiles, relative density, and pore morphology [29–31]. Finally, it is noted that $E_{d,\mathrm{eff}}$ and $\mathrm{VED_M}$ are scalar descriptors. Accordingly, beam-shape effects are interpreted alongside the measured beam intensity profiles.

The initial parameter range was guided by our previous single-track and cube studies on beam-shaped PBF-LB/M Ti-6Al-4V and by relevant literature on beam-profile-dependent process-window development [32,33]. For all beam modes, laser power, scan speed, and a common hatch-spacing range were investigated to cover low, intermediate, and high $\mathrm{VED_M}$ regimes. Because the beam profiles had different effective diameters and intensity distributions, the same hatch spacing corresponded to different relative melt-track overlap conditions across modes. Representative tensile conditions were then selected based on the resulting relative density and pore morphology.

Table 1
Measured 2D beam profiles and corresponding beam diameters.

Parameters	Power ratio (core/ring)		
	Gaussian	Mode 3 (49/51)	Mode 6 (9/91)
2D beam profile	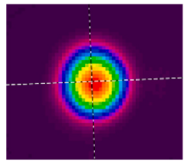	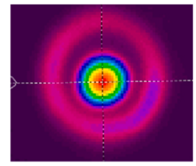	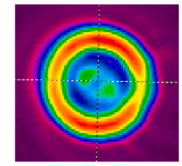
Nominal beam width (μm)	81	163	210
Equivalent beam diameter, $D_{0.1,\ eq}$ (μm)	87.01	179.75	229.15

Table 2
Summary of processing conditions and specimen geometries.

Parameter	Values
Machine	AMCM M290–2 FLX (nLIGHT AFX laser−1000 beam shaping)
Beam modes	Mode 0 (M0), Mode 3 (M3), Mode 6 (M6)
Laser power, P (W)	200–500
Scan speed, v (mm/s)	450–650 (mode-dependent combinations)
VED range (J/mm^3)	51–206
Hatch spacing, h (μm)	80–200
VED_M ($Jmm^{-2}s^{-1/2}$)	132–332
Layer thickness, t (μm)	30 μm
Specimen Type 1	Standard Cubes 10 × 10 × 10 mm^3
Specimen Type 2	Cylindrical rods (Ø8 mm × 92 mm, no threads) for miniature tensile extraction

2.3. *Materials characterization and mechanical testing*

Internal defects were quantified non-destructively by μCT using a Diondo Evo05 (Diondo GmbH, Germany) at 150 kV, 66 μA, 190 ms integration time, and 15 μm voxel size. Reconstructed volumes (cubes and tensile specimens) were analyzed in VGSTUDIO MAX (Volume Graphics GmbH, Germany) for pore segmentation and pore-statistics extraction. Cubes were sectioned at mid-height for metallographic examination using a Discoton 6 cutter, cold-mounted in epoxy (ClaroCit kit, Struers GmbH), and prepared using a Tegramin−30 system. Grinding was performed with SiC papers (80–2500 grit), followed by polishing using DIADUO−2 diamond suspensions (9, 3, 1 μm) and final polishing with OP-S/OP-U to achieve a mirror finish. Selected samples were etched using Kroll's reagent (5 vol% HNO_3, 2 vol% HF) for 10–12 s. Optical microscopy and 3D laser scanning confocal microscopy (VK-X160K, Keyence, Japan) were used for the microstructure and pore/feature visualization.

To link the beam-shape-dependent porosity regimes with mechanical response, tensile testing was conducted using miniature flat dog-bone specimens (overall length 20 mm) machined from the Ø8 mm × 92 mm rods, which served as parent printed blanks and were not directly tested as cylindrical tensile specimens. The flat geometry was selected to satisfy the dimensional constraints of the elevated-temperature gripping/furnace setup and to allow multiple specimens to be extracted from the same printed rod. The specimens were extracted from the top central region of the rods, with the tensile axis aligned parallel to the build direction (Fig. 1). The cylindrical rods were sectioned into ~1.3 mm plates and mechanically polished on both sides to a final thickness of around 1.0 mm. Four specimens were obtained from each rod, of which three were tested, and one was retained as a spare/reference. The final gauge width and thickness were measured individually after polishing, and engineering stress was calculated from the initial measured gauge cross-section of each specimen, $S_0 = w \times t$, where w is the gauge width and t is the final polished gauge thickness. Tensile testing followed the general procedures of ASTM E8/E8M and ISO 6892–1 for room-temperature testing, and ASTM E21/ISO 6892–2 for elevated-temperature testing. Tensile tests were performed at RT, 200 °C, and 400 °C using an Instron 5982 universal testing machine. These temperatures were selected to provide a room-temperature reference condition and two elevated-temperature conditions relevant to the thermomechanical response of Ti-6Al-4V. Specifically, 200 °C was used as an intermediate elevated-temperature condition, while 400 °C was selected as an upper service-relevant benchmark where thermal softening and defect-assisted damage evolution become more pronounced in Ti-6Al-4V, as reported in previous elevated-temperature tensile studies [34–36]. Room-temperature tests were conducted at a crosshead displacement rate of 0.05 mm min^{-1} (8.33 × 10^{-7} m s^{-1}), with strain measured by digital image correlation (DIC). Elevated-temperature tests used the same specimen geometry, where the samples were heated and held isothermally prior to loading and then tested at a crosshead displacement rate of 0.10 mm min^{-1} (1.67 × 10^{-6} m s^{-1}). The same specimen geometry, extraction direction, surface preparation, and cross-sectional area measurement procedure were used for all tested conditions. For each tested condition, $n = 3$ specimens were tested. The core–ring (M3) condition was included in beam characterization and porosity/density mapping, while tensile testing was performed for M0 and M6.

Polished surfaces and (where applicable) fracture surfaces were examined using a ZEISS scanning electron microscope (SEM). Microstructure images were acquired in BSE (BSD1) at 15 kV and a working distance (WD) of 10.9 mm, while fracture-surface imaging was performed in secondary-electron mode (SE2) at an accelerating voltage of 10 kV. Relative density was determined primarily from OM cross-sections for reporting/plotting and independently supported by μCT-based porosity (pore volume fraction from segmented μCT volumes converted to porosity/relative density). OM/confocal images were used additionally for qualitative defect visualization and morphology assessment, although thin planar lack-of-fusion defects remain orientation-sensitive in 2D sections.

3. Results and discussion

3.1. *Beam-shape effects on relative density and porosity (mapped by VED_M)*

Figs. 2–3 show that the modified energy metric VED_M captures a clear beam-shape-dependent defect window in PBF-LB/M Ti-6Al-4V. Depending on the spatial energy distribution (M0 vs M3 vs M6), the dominant porosity shifts from lack-of-fusion at lower input to keyhole-type porosity at higher input. In the 3D μCT reconstructions (Fig. 2), pores are characterized using geometric descriptors (sphericity ψ and equivalent diameter). Low-ψ pores are used here as indicators of

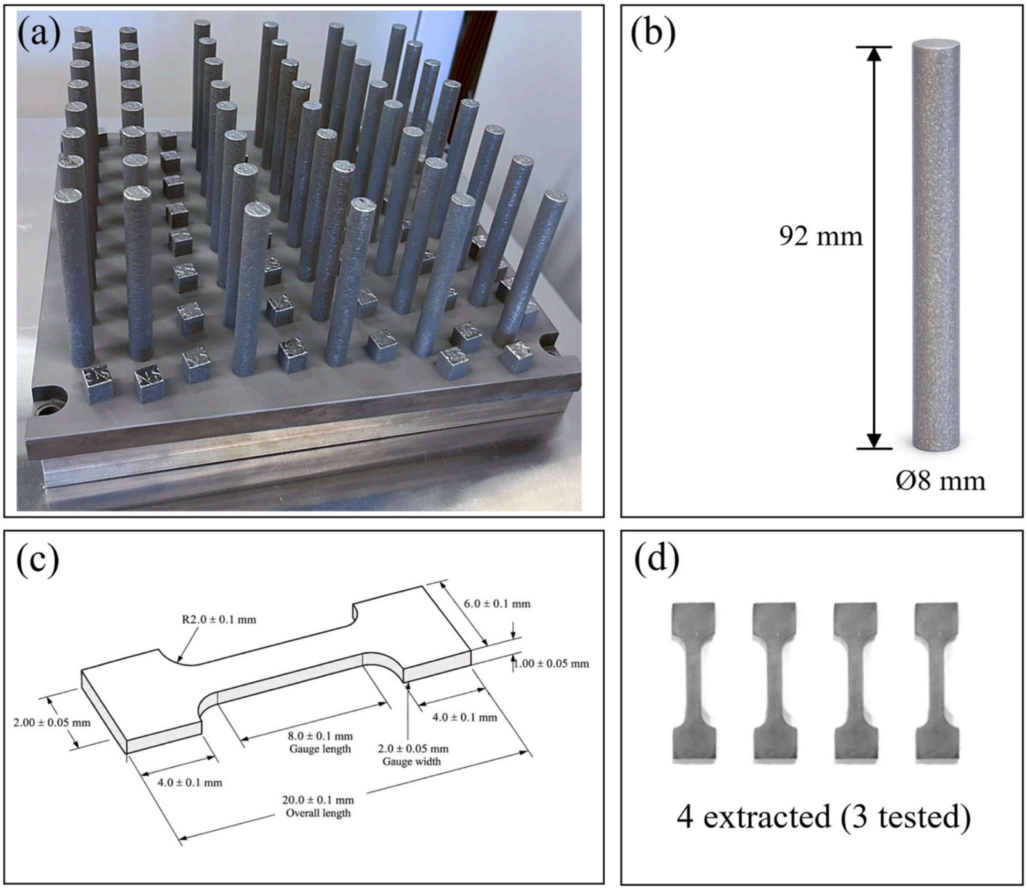

Fig. 1. PBF-LB/M build job and specimen preparation: (a) density cubes and rods, (b) as-built rod, (c) dimensioned miniature flat dog-bone geometry for elevated-temperature tensile testing, and (d) four specimens extracted per rod.

irregular/LoF-like defects, whereas higher-ψ pores are more consistent with keyhole-/gas-type morphologies. The polished cross-sections (Fig. 3) provide complementary 2D validation of these morphology trends. Importantly, the μCT analysis primarily resolves pores above the voxel-scale threshold (≈15 μm), and sub-resolution metallurgical microporosity is therefore not captured. Therefore, the discussion below emphasizes the process-induced defects that control density, rather than sub-resolution metallurgical microporosity.

At the lower investigated energy input ($VED_M = 222$ J mm^{-2} s$^{-1/2}$), the Gaussian mode (M0) remains near-fully dense, whereas the redistributed profiles move closer to the lack-of-fusion (LoF) boundary (Figs. 2–3, $VED_M = 222$ row). In this row, M3 contains only a small number of defects, while M6 shows a substantially higher pore population with irregular and locally interconnected defect regions. Although some pores in the 2D section appear rounded, the combined OM and μCT results indicate that the defect population in M6 is dominated by LoF-related porosity, in contrast to the more rounded pores observed for M0 at high VED_M, which are more consistent with keyhole-/gas-type porosity. Overall, these results show that more substantial energy redistribution increases LoF susceptibility at low VED_M, while the Gaussian mode remains stable within the investigated window, which supports the previous similar findings [32,33].

At intermediate input ($VED_M \approx 285$), all three beam modes approach a high-density regime with only limited residual porosity in both μCT and polished cross-sections (Figs. 2–3, $VED_M \approx 285$ row). A localized LoF-affected region is still visible for M6 in the μCT volume, indicating that, under the selected hatch spacing, spatially confined lack-of-fusion features can persist even when the overall density is high and melt-track overlap is only marginal. More generally, this result shows that a single bulk-density value may not fully capture proximity to the LoF boundary in near-threshold conditions.

When VED_M is further increased to 332, M0 shows a clear shift toward a keyhole-type porosity signature. The μCT reconstruction indicates a population of more compact, higher-sphericity pores (Fig. 2, $VED_M = 332$, M0 column), and the polished cross-section shows a dense distribution of rounded pores (Fig. 3, same condition). This behavior is consistent with excessive local energy input under a centrally peaked intensity profile, promoting deeper melt pools and keyhole-like instability. In contrast, both M3 and M6 remain nearly fully dense at the same high VED_M (Figs. 2–3, bottom-middle/right), demonstrating that radial energy redistribution suppresses keyholing by lowering the local peak intensity while maintaining sufficient melt overlap. In practical terms, beam shaping therefore delays keyhole onset at high VED_M, even though it can increase LoF susceptibility at the lowest VED_M.

Fig. 4 quantitatively consolidates the μCT/sectional observations by plotting relative density against VED_M. Two distinct trends emerge. M3 and M6 densify monotonically with increasing VED_M and approach a near-full-density plateau (≈99.9%) at the upper end of the window. In contrast, M0 shows the reverse behavior: high density is already obtained at low-to-intermediate VED_M, followed by a monotonic decrease at the highest VED_M, consistent with the high-energy pore regime observed in Figs. 2–3. The larger scatter at the lowest VED_M points further reflect the increased sensitivity of redistributed modes near the densification threshold [37].

Taken together, Figs. 2–4 establish a beam-shape-dependent densification window when mapped by VED_M. The redistributed profiles (M3/M6) mitigate density loss at the high-VED_M end, consistent with suppression of compact/keyhole-consistent pore populations, whereas the M0 shows a clear high-VED_M instability reflected by reduced relative density. Conversely, the redistributed modes are primarily constrained

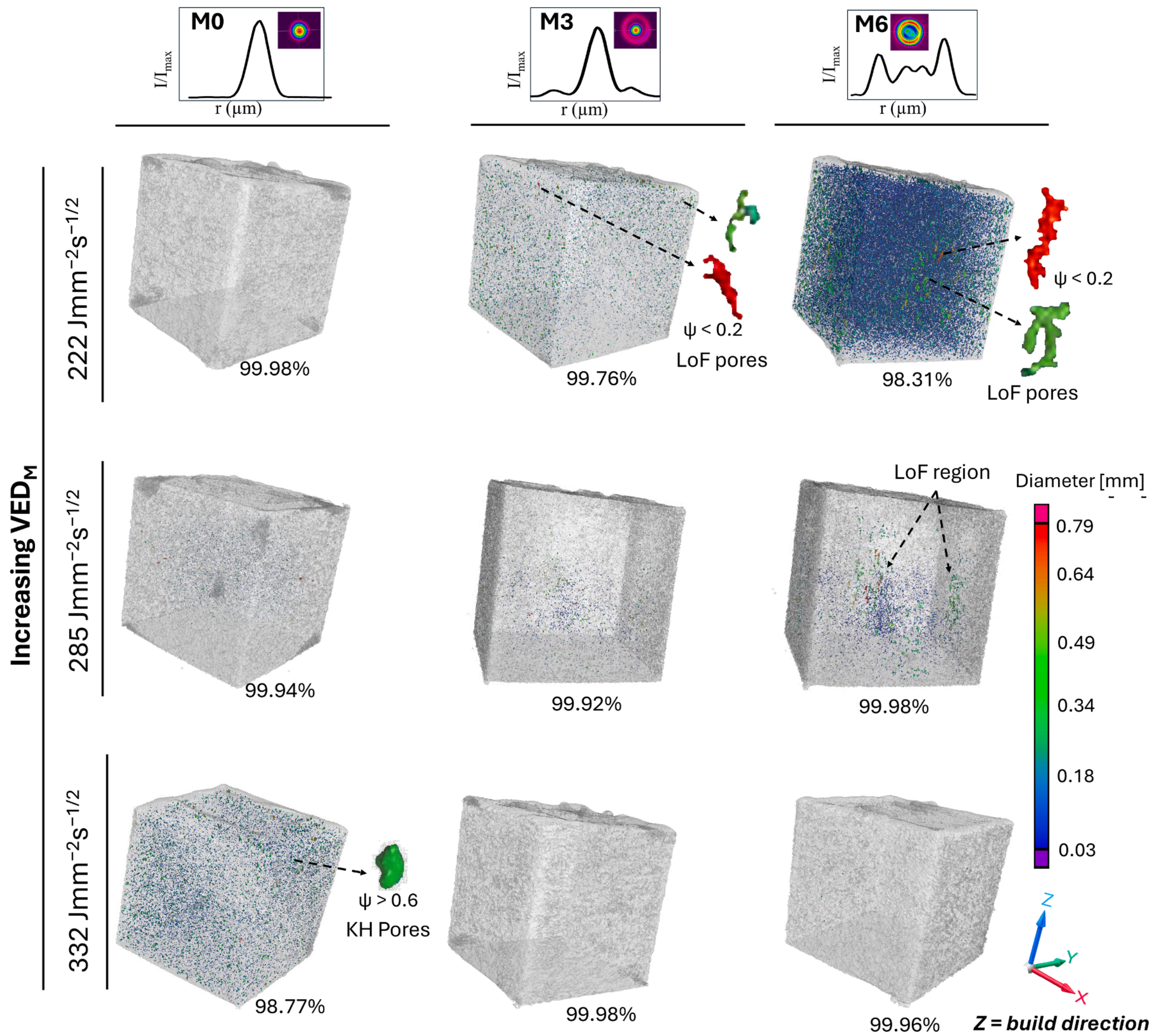

Fig. 2. μCT 3D reconstructions of Ti-6Al-4V cubes produced with M0, M3, and M6 at increasing normalized energy metric VED_M (J mm^{-2} $s^{-1/2}$) (top to bottom). Pore distribution and morphology are visualized by equivalent diameter; low-sphericity irregular pores are LoF-like, while compact/high-sphericity pores are consistent with keyhole-/gas-type porosity.

near the low-VED_M boundary where LoF-like defects appear. This VED_M based defect–density map provides the rationale for selecting representative tensile conditions discussed next.

3.2. High-temperature tensile response and fracture mechanisms

High-temperature performance of PBF-LB/M Ti-6Al-4V is particularly sensitive to process-induced porosity, since pores act as stress concentrators and can accelerate damage growth during thermally activated plastic flow [38,39]. More broadly, studies on designed porous Ti-6Al-4V structures also show that pore architecture and morphology can influence macromechanical performance, supporting the need to consider pore characteristics beyond relative density alone [40]. To link the beam-shape-dependent defect window (Section 3.1) with tensile behavior, the as-built cylindrical tensile specimens were first evaluated by μCT within the gauge region. Fig. 5 compares pore populations in tensile bars produced at a common high normalized energy input (VED_M=332 $Jmm^{-2}s^{-1/2}$) for the three beam profiles. This condition was selected to compare the defect states that developed under the same nominal processing metric at the upper end of the investigated window. Despite the matched VED_M, M0 exhibits the lowest relative density (≈98.56%) and the highest pore number density throughout the scanned length, whereas M3 and M6 achieve substantially higher densities (≈99.85% and ≈99.81%, respectively) with markedly fewer porosity defects. The diameter–sphericity maps show a wider pore-size distribution for M0, with a higher fraction of porosity defects, whereas M3 and M6 cluster toward smaller pores. Slightly lower rod density (compared to cubes) is attributed to geometry and scan path-dependent thermal history, and the higher contribution of contour/near-surface regions in the evaluated volume [41]. Overall, these μCT results define the defect state for interpreting the tensile and fracture results that follow.

M0 and M6 were selected for tensile testing as end-member beam profiles, providing the strong contrast between Gaussian/core-dominated and ring-dominated energy distributions. M3 was retained as an intermediate condition for beam characterization, density/porosity mapping, and μCT gauge-region analysis, but was not included in the focused tensile matrix because its high-VED_M density response was close to M6. Fig. 6 compares the engineering stress–strain responses of M0 and M6 at two energy input levels and three temperatures (RT, 200 °C, and 400 °C). In all cases, increasing temperature causes the expected thermal softening, reflected by lower peak stress and reduced work-hardening [42,43], while the strain to failure varies with beam mode and processing condition. For the high VED_M condition, the μCT scans of the CT-scanned gauge region (Fig. 5) show a substantially higher defect burden in M0 than in the ring-dominated mode. This

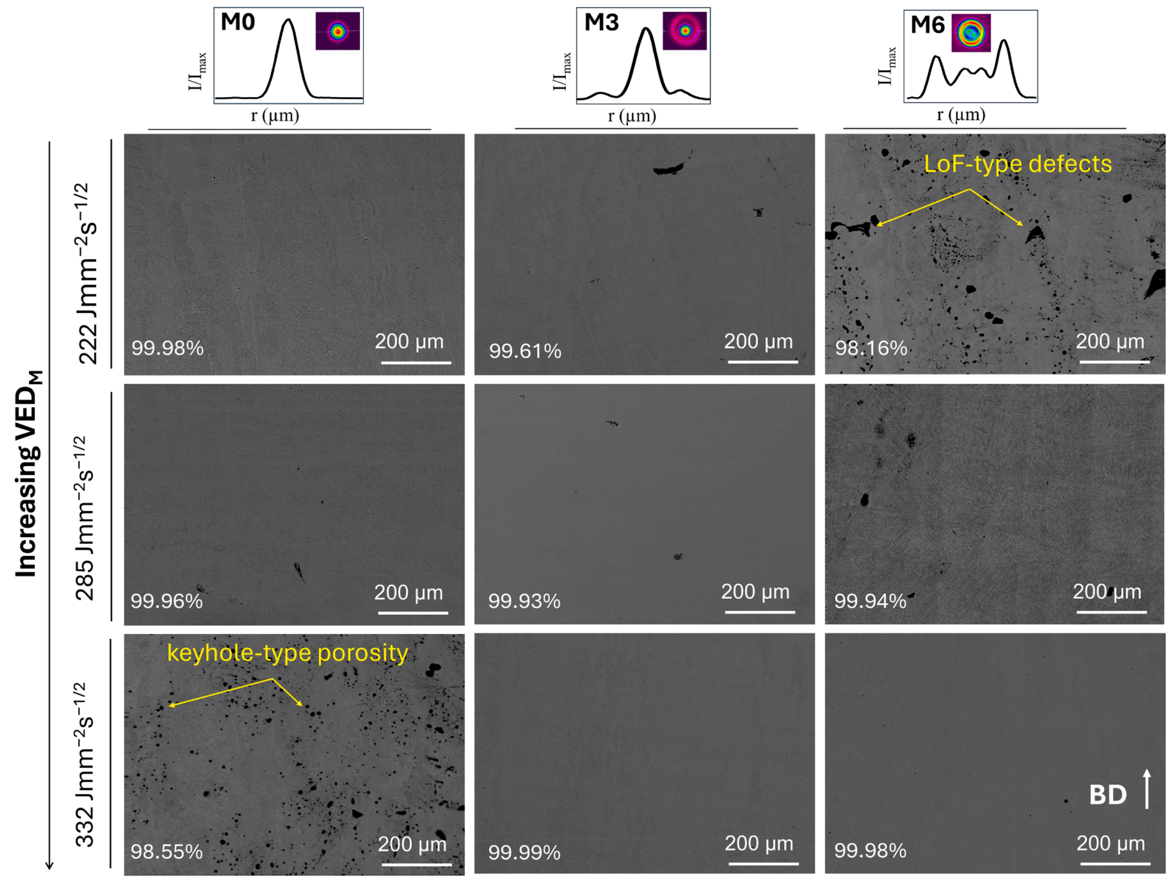

Fig. 3. Representative polished cross-sections of the same cube builds (M0, M3, M6) at increasing VED$_M$ (J mm^{-2} s$^{-1/2}$) (top to bottom), showing the transition from LoF-like defects at low VED$_M$ to compact pore populations at high VED$_M$ depending on the beam mode. BD denotes the build direction.

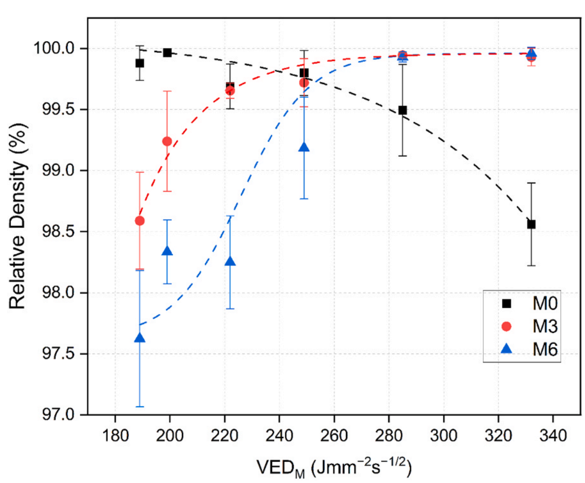

Fig. 4. Relative density as a function of VED$_M$ for M0, M3, and M6, summarizing the beam-shape-dependent densification window. Data points show mean relative density from three representative polished-surface regions. Error bars indicate the corresponding regional standard deviation. Dashed lines represent DoseResp trend fits applied consistently to all three datasets and are intended only to visualize the overall trends.

difference is consistent with an increased tendency for earlier damage localization from critical pores, particularly at elevated temperature [44,45], although microstructural contributions cannot be excluded. Representative etched OM images were added in the supplementary file (Fig. S2) to provide qualitative microstructural context beyond pore marking. M6 shows more continuous and aligned prior-β columnar features along the build direction, whereas M0 shows a higher visible pore burden and less continuous prior-β morphology. This is consistent with recent studies showing that laser thermal-profile engineering can modify grain architecture, ductility, and α/α′/β evolution in AM Ti-6Al-4V [46,47]. Our recent SEM/EBSD study on the same beam profiles further showed that beam shaping affects prior-β grain continuity, alignment, crystallographic texture, and α′ lath organization, while no retained β phase was detected at room temperature within the EBSD resolution [32]. Taken together, these observations suggest that the higher retained ductility of M6 at elevated temperature is primarily associated with its lower critical-pore burden, with possible support from more continuous prior-β/α′ microstructural organization. Therefore, the present tensile response is interpreted primarily in relation to the measured defect state, while possible contributions from beam-shape-induced prior-β grain morphology, texture, and α′ lath organization are also acknowledged.

For M0 at moderate energy of 285 Jmm^{-2}s$^{-1/2}$ (Fig. 6a), the curves show a progressive loss in strength and a concurrent increase in ductility with temperature. Table 3 quantifies this trend: the peak engineering stress decreases from 1150 ± 37 MPa (RT) to 942 ± 20 MPa (200 °C) and 871 ± 18 MPa (400 °C), while strain increases from 5.0 ± 0.5% to 6.6 ± 1.0% and 12.5 ± 0.5%, respectively. In contrast, M0 at high energy (Fig. 6b) exhibits a markedly reduced strain capacity at elevated temperatures despite a comparable RT strain to failure. The strain remains at 5 ± 2% at 200 °C and reaches only 7 ± 1% at 400 °C, while the corresponding peak stresses are 1111 ± 67 MPa and 956 ± 8 MPa (Table 3). When considered alongside the porosity results in Figs. 2–5, the reduced strain capacity of high-energy M0 is consistent with earlier damage localization from critical pores. At the same time, the retained

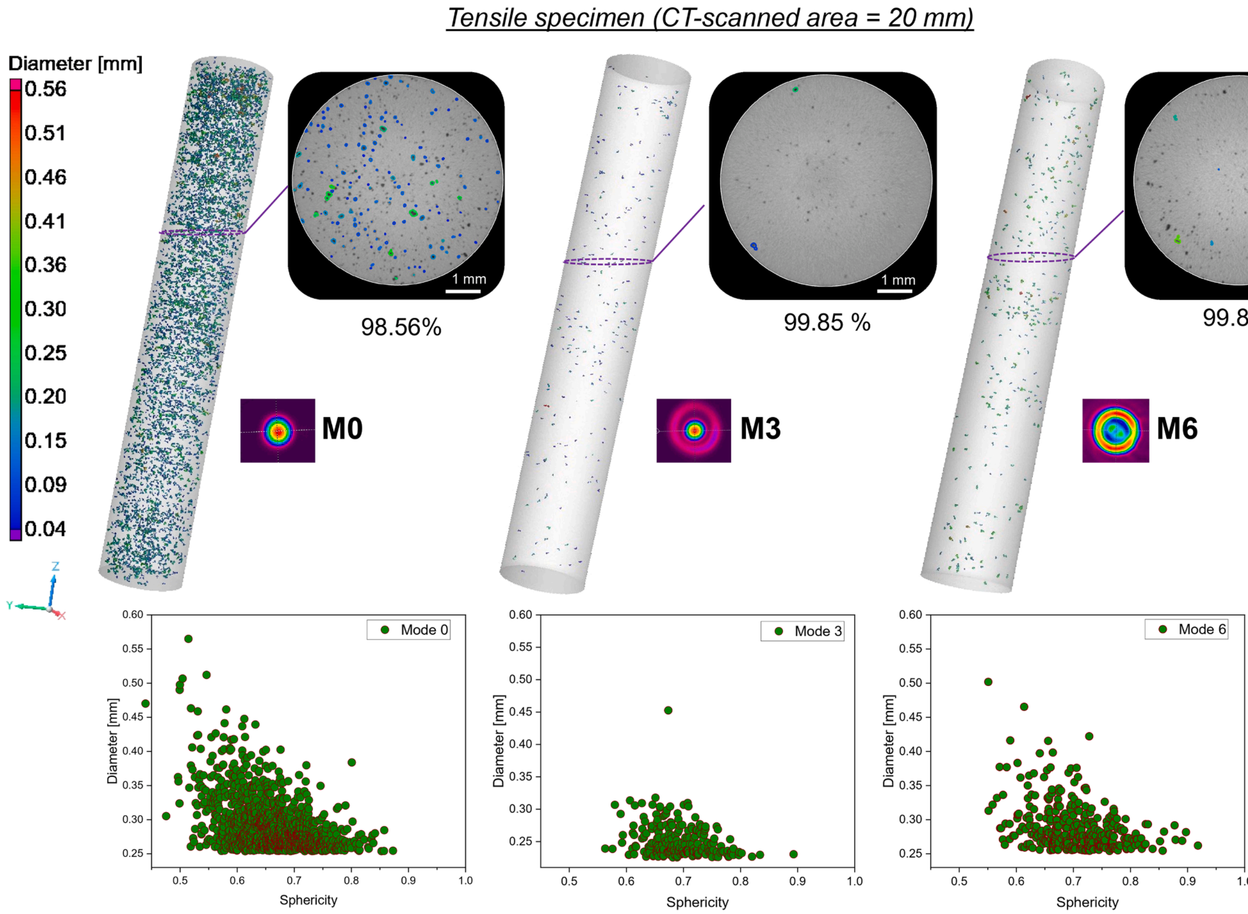

Fig. 5. Representative μCT reconstructions of the scanned tensile gauge region (20 mm) for M0, M3, and M6 specimens at the high-VED$_M$ condition (VED$_M$ = 332 J mm^{-2} s$^{-1/2}$), with pores colored by equivalent diameter. The diameter–sphericity plots show the pore size and shape distributions within the selected scanned gauge regions for each beam profile.

high peak stress indicates that porosity alone does not fully explain the response, and microstructural contributions may also be involved. Thus, the pore population appears to mainly limit ductility by promoting earlier void growth and coalescence, whereas the peak stress is comparatively less sensitive and may also reflect microstructural effects.

M6 shows higher retained ductility at elevated temperature than M0, indicating a more stable plastic response under the compared conditions. At moderate energy (Fig. 6c), M6 achieves a substantial ductility increase at temperature: strain rises from 5.2 ± 0.7% (RT) to 12 ± 0.3% (200 °C) and 13.4 ± 0.5% (400 °C), while peak stress drops from 1130 ± 38 MPa to 920 ± 15 MPa and 747 ± 10 MPa (Table 3). At high energy (Fig. 6d), M6 maintains a similar RT strain (5 ± 1%) but still retains high ductility at temperature (11 ± 3% at 200 °C and 10.1 ± 1.1% at 400 °C), with peak stresses of 938 ± 10 MPa and 921 ± 33 MPa, respectively. Overall, Table 3 and Fig. 6 indicate that, under the compared conditions, the ring-dominated profile retains higher ductility at elevated temperature than the Gaussian profile, without a major penalty in peak stress. This trend is consistent with the shifted defect window discussed in Section 3.1 and, for the high VED$_M$ condition, with the lower defect burden observed in the CT-scanned gauge region for M6 than for M0 (Fig. 5). However, the present results indicate that defect population is most clearly associated with ductility and damage evolution, whereas peak stress may additionally reflect beam-shape-induced microstructural differences. Accordingly, the tensile comparison should be interpreted as the response of specimens with different beam-shape-dependent defect states generated under the selected processing conditions, rather than as a strict isolation of beam-shape effects independent of porosity or microstructure.

The tensile values obtained in this study are broadly consistent with reported data for PBF-LB/M or DMLS Ti-6Al-4V tested at room and elevated temperatures. Previous studies have shown that L-PBF/DMLS Ti-6Al-4V retains relatively high strength up to intermediate temperatures, while increasing temperature generally causes thermal softening and can improve ductility depending on defect state, phase constitution, and heat treatment condition [34–36]. In the present work, the RT peak stresses of M0 and M6 remain within the high-strength range expected for PBF-LB/M Ti-6Al-4V, and the 200–400 °C tests show the expected reduction in peak stress. Compared with the literature, the beam-shape effect is therefore more evident in densification and ductility retention than in a uniform increase in tensile strength. At the high VED$_M$ condition, M6 retained higher ductility at 400 °C than M0 while maintaining comparable peak stress, consistent with its lower measured defect burden. This also agrees with our recent beam-shaping study on Ti-6Al-4V, where the ring-dominated profile achieved near-full density and a favourable indicative strength–ductility balance (at RT) under optimized conditions [32].

The fracture-surface observations help rationalize how the observed defect states may contribute to damage initiation and final failure at RT and 400 °C. Considered together with the μCT porosity maps, cross-sectional microscopy, and the stress–strain response (Figs. 5–6 and Table 3), the fractography supports a shift from more defect-sensitive fracture in the Gaussian condition (M0) toward more uniformly ductile tearing in the ring-dominated condition (M6), particularly for the higher-energy tensile builds.

M0 (Fig. 7) shows numerous exposed voids on the fracture surface at both RT and 400 °C, indicating that process-induced pores intersect the

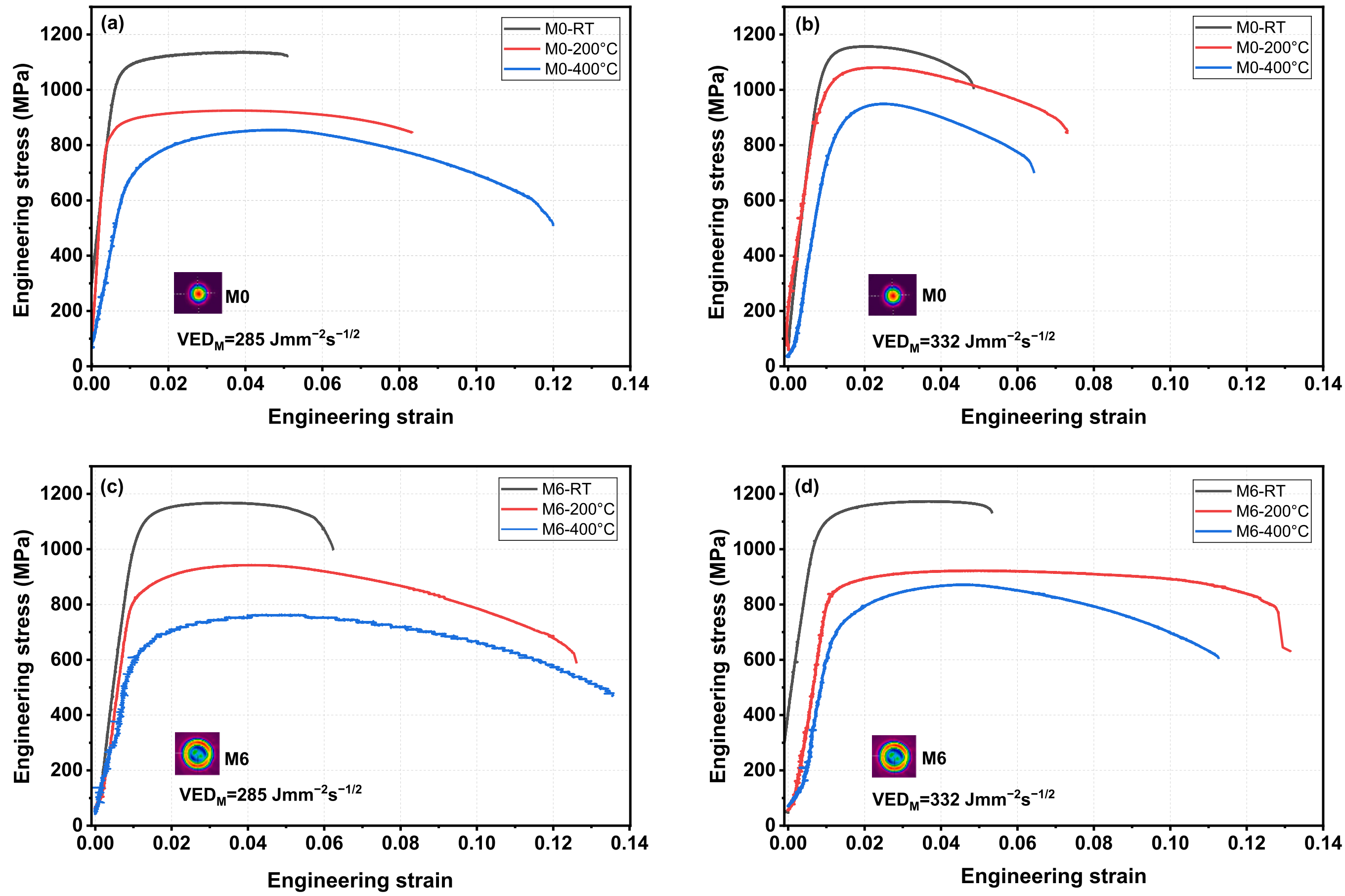

Fig. 6. Engineering stress–strain curves at RT, 200 °C, and 400 °C for M0 (a–b) and M6 (c–d) produced at two normalized energy input levels (VED_M = 285 and 332 $Jmm^{-2}s^{-1/2}$). The curves illustrate temperature-dependent softening and the corresponding differences in the stable plastic regime and strain to failure for the compared processing conditions.

Table 3
Average peak stress and strain to failure (RT–400 °C): Mode 0 vs Mode 6 at two VED_M levels.

Beam Profile/ Energy input	Temperature (°C)	Strain (%)	Stress (MPa)
M0 (Moderate VED_M)	25 (RT)	5 ± 0.5	1150 ± 37
	200	6.6 ± 1	942 ± 20
	400	12.5 ± 0.5	871 ± 18
M0 (High VED_M)	25 (RT)	5 ± 0.9	1196 ± 38
	200	5 ± 2	1111 ± 67
	400	7 ± 1	956 ± 8
M6 (Moderate VED_M)	25 (RT)	5.2 ± 0.7	1130 ± 38
	200	12 ± 0.3	920 ± 15
	400	13.4 ± 0.5	747 ± 10
M6 (High VED_M)	25 (RT)	5 ± 1	1177 ± 28
	200	11 ± 3	938 ± 10
	400	10.1 ± 1.1	921 ± 33

crack path and reduce the effective load-bearing ligaments. At RT (Fig. 7a), the high-magnification view reveals a large, near-rounded pore surrounded by dense ductile dimples. The internal solidified feature within the cavity is consistent with a keyhole-type pore containing trapped/re-solidified melt, and the surrounding dimpled morphology indicates microvoid coalescence in the ligaments. Such a pre-existing cavity acts as a local stress concentrator, promoting earlier void growth and coalescence and therefore pore-assisted damage initiation [48,49]. This interpretation agrees with the porosity maps (Figs. 2–5), where M0 at higher energy input shows a more severe pore population, and with the tensile response, where high peak stress can coincide with curtailed strain due to early localization at critical defects.

At 400 °C (Fig. 7b), the fracture surface remains mostly ductile, showing microvoid coalescence with equiaxed and locally shear-influenced (parabolic) dimples, while exposed process-induced pores persist on the fracture plane (including keyhole-consistent cavities). This suggests that elevated temperature promotes plastic flow and tearing but does not eliminate pore-assisted damage initiation, consistent with the ductility-limited behavior of M0, as also reflected in the tensile metrics (Table 3), the higher pore population revealed by µCT (Fig. 5), and the stress–strain response (Fig. 6).

In contrast to M0, M6 exhibits fracture features consistent with a more uniformly ductile failure process and a reduced influence of critical process pores. At both RT and 400 °C, the low-magnification views show a pronounced necking region, indicating that failure is preceded by substantial plastic deformation rather than being dominated by premature fracture from a single large defect. At RT (Fig. 8a), the fracture surface is populated by dense, relatively homogeneous fields of equiaxed dimples and microvoid coalescence features, consistent with distributed void nucleation and stable growth/coalescence. No large cavity analogous to the keyhole-consistent pore observed for M0 is evident in the imaged region, which agrees with the µCT gauge scans showing a lower pore population for M6 than M0 (Fig. 5). This defect state supports the more stable deformation response seen in the stress–strain curves and the strength–ductility balance summarized in Table 3.

At 400 °C (Fig. 8b), the fracture morphology remains ductile but shifts toward elongated dimples, tearing ridges, and clear plastic-flow features. This change is consistent with reduced flow stress and enhanced plasticity at elevated temperature, which increases the

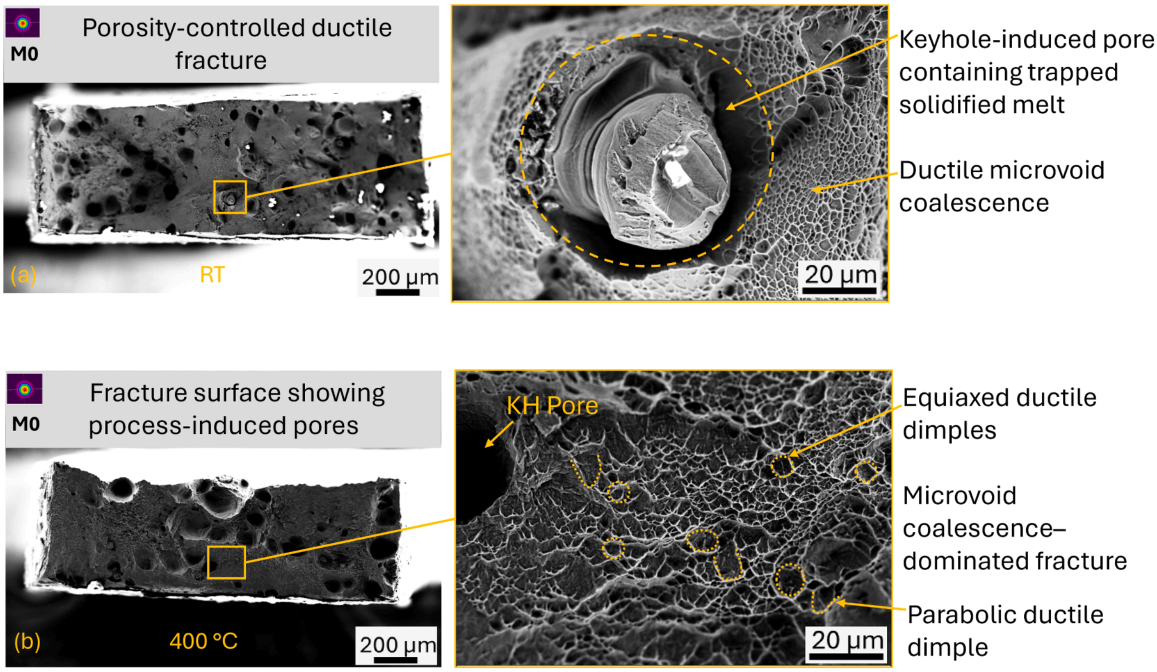

Fig. 7. SEM fractographs of M0 (Gaussian) tensile specimens tested at (a) RT and (b) 400 °C, showing exposed process-induced pores and a largely ductile dimpled fracture morphology (microvoid coalescence).

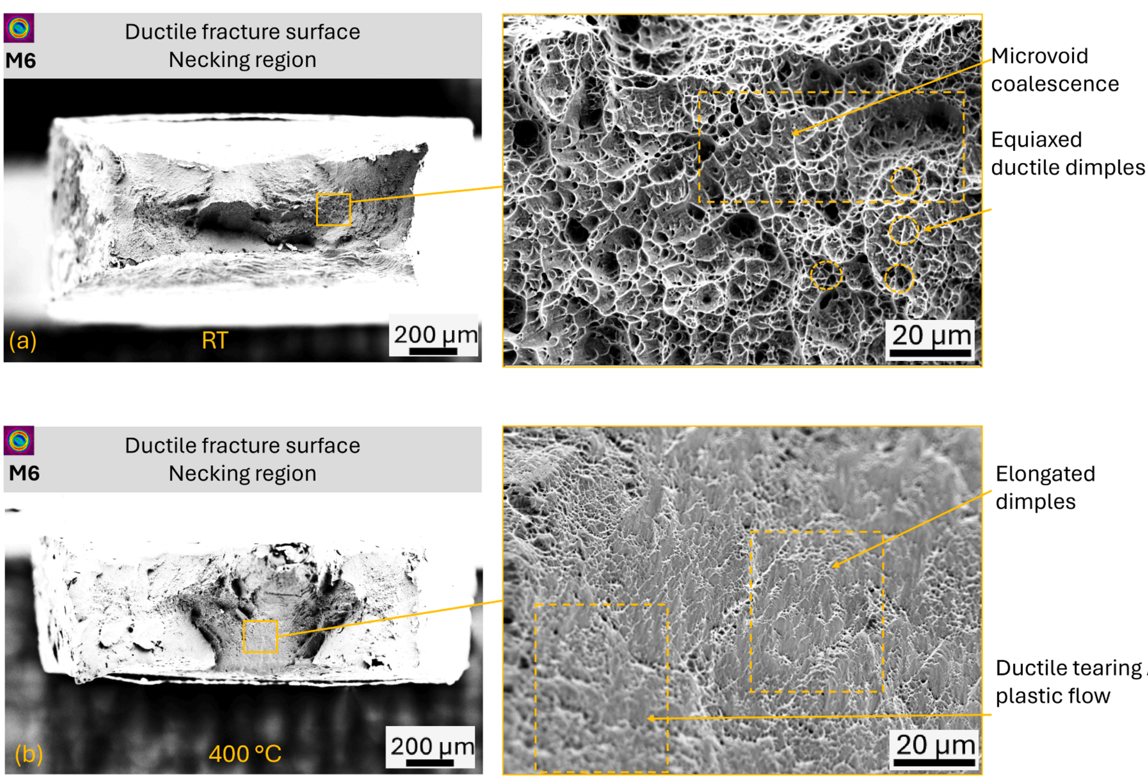

Fig. 8. SEM fractographs of M6 (ring-dominated) tensile specimens tested at (a) RT and (b) 400 °C, showing ductile fracture with pronounced necking and dimpled microvoid coalescence (more elongated dimples and tearing features at 400 °C).

contribution of shear to final fracture. Importantly, large process-induced pores are not widely exposed on the fracture plane at 400 °C, suggesting a greater contribution from ductile tearing of the matrix, rather than clear evidence of widespread pore-triggered rupture in the imaged region. Overall, the fractography is consistent with a more defect-sensitive fracture response in M0, including pore-assisted damage initiation, whereas M6 shows a more uniformly ductile microvoid-coalescence/tearing morphology under both RT and elevated-temperature loading.

4. Limitations and future outlook

While this study provides a coherent framework for discussing process–defect–property relationships through beam-profile characterization, μCT/OM/SEM, and RT–400 °C tensile testing, several limitations should be noted. The modified/normalized energy metric VED_M was shown to be useful for comparing beam modes, but it remains a reduced-order descriptor and does not explicitly capture absorptivity variations, transient melt-pool flow, keyhole stability, or spatter/denudation. Its physical basis could therefore be strengthened in the future by in-situ monitoring and/or validated thermal–fluid simulations. In addition, the parameter space was sampled through representative low–mid–high conditions for porosity mapping and two build conditions for tensile testing, so the reported process windows are valid within the investigated range, scan strategy, and geometries. Because the compared beam modes did not produce identical defect states under all tensile-testing conditions, the present results do not fully isolate beam-shape effects from defect-population effects.

The μCT voxel size (15 μm) enables robust quantification of dominant pores but may under-resolve sub-voxel defects. Therefore, higher-resolution scans and segmentation sensitivity checks would further refine pore statistics, especially near full density. Finally, tensile testing was limited to RT, 200 °C, and 400 °C, with the available repeat count and without a systematic build-orientation, post-processing, or matched-defect-state comparison matrix. In addition, tensile testing was focused on the M0 and M6 end-member beam profiles, while M3 was retained for beam characterization and porosity/density mapping. Future work should therefore expand repeats, include intermediate beam-profile conditions in mechanical testing, assess anisotropy and heat-treatment effects, add quantitative fractography, and perform more systematic EBSD/XRD-based microstructure and texture characterization. In particular, tensile comparisons at more closely matched density/defect levels across beam modes would help decouple defect-population effects from beam-shape-induced microstructural variations, especially in relation to peak stress and damage evolution.

5. Conclusion

This study links beam shaping to porosity regimes and the resulting tensile response of PBF-LB/M Ti-6Al-4V at room and elevated temperatures. The key findings are as follows:

1. Core–ring and ring-dominated profiles progressively suppress LoF defects with increasing energy input, whereas the Gaussian mode shows an optimum densification window and then shifts toward a keyhole-type porosity signature at the highest input, accompanied by density loss.
2. At nominally comparable energy input, the tensile gauge regions exhibited different pore populations across beam modes, establishing distinct initial defect states for mechanical loading.
3. All conditions exhibit thermal softening with increasing temperature, but strain to failure is most clearly associated with pore type and severity rather than density alone. Beam shaping does not uniformly increase strength or ductility; instead, it shifts the strength–ductility balance through changes in the severity of critical pores, while possible microstructural contributions are also acknowledged. The Gaussian profile at high VED_M maintains high peak stress yet shows curtailed ductility, consistent with earlier localization at critical pores, whereas the ring-dominated profile retains ductility more consistently in line with its lower measured defect burden and more stable microstructural features.
4. Fractography is consistent with a more defect-sensitive fracture response in the Gaussian condition, including pore-assisted damage initiation, whereas the ring-dominated condition shows a more uniformly ductile tearing morphology.

CRediT authorship contribution statement

Abid Ullah: Conceptualization, Writing – review & editing, Writing – original draft, Visualization, Validation, Software, Methodology, Investigation, Funding acquisition, Formal analysis, Data curation. **Amjad Iqbal**: Writing – review & editing, Visualization, Validation, Software, Methodology, Investigation, Data curation. **Kai Zhang**: Writing – review & editing, Funding acquisition. **Tingting Liu**: Writing – review & editing, Supervision. **Dirk Herzog**: Writing – review & editing, Supervision, Project administration. **Alexander E. Medvedev**: Writing – review & editing, Supervision. **Andrey Molotnikov**: Writing – review & editing, Supervision. **Ingomar Kelbassa**: Writing – review & editing, Supervision. **Milan Brandt**: Writing – review & editing, Validation, Supervision, Formal analysis.

Declaration of Competing Interest

The authors declare that they have no known competing financial interests or personal relationships that could have appeared to influence the work reported in this paper.

Acknowledgements

This project has received funding from the European Union's Horizon 2020 research and innovation program under the Marie Skłodowska-Curie grant agreement No 101034328. This paper reflects only the author's view, and the Research Executive Agency and the European Commission are not responsible for any use that may be made of the information it contains. This work was also supported by the National Natural Science Foundation of China (Grant No. 52005262) and the National Key Research and Development Program of China (Grant No. 2022YFB4600800).

Appendix A. Supporting information

Supplementary data associated with this article can be found in the online version at doi:10.1016/j.mtcomm.2026.115701.

Data Availability

Data will be made available on request.

References

[1] A. Bulloch, A. Cruchley, A. Groom, A. Harris, F. Schulz, C.J. Tuck, R. Hague, M. Simonelli, Effect of interface orientation in laser powder bed fusion of IN718/GRCop-42 bimetallic parts for Aerospace, Addit. Manuf. Lett. 15 (2025) 100331, https://doi.org/10.1016/j.addlet.2025.100331.

[2] S.-H. Lee, J.-H. Koo, O. Cakmak, J.-W. Cho, Effect of laser power during laser powder bed fusion on microstructure of joining interface between Tungsten and AISI 316L steel, Addit. Manuf. Lett. 11 (2024) 100246, https://doi.org/10.1016/j.addlet.2024.100246.

[3] Q. Gaillard, X. Boulnat, S. Cazottes, S. Dancette, C. Desrayaud, Strength/ductility trade-off of Laser Powder Bed Fusion Ti-6Al-4V: Synergetic effect of alpha-case formation and microstructure evolution upon heat treatments, Addit. Manuf. 76 (2023) 103772, https://doi.org/10.1016/j.addma.2023.103772.

[4] J. Reijonen, A. Revuelta, S. Metsä-Kortelainen, A. Salminen, Effect of laser focal point position on porosity and melt pool geometry in laser powder bed fusion additive manufacturing, Addit. Manuf. 85 (2024) 104180, https://doi.org/10.1016/j.addma.2024.104180.

[5] A. Ullah, A. Ur Rehman, M.U. Salamci, F. Ptr, T. Liu, The influence of laser power and scanning speed on the microstructure and surface morphology of Cu2O parts in SLM, Rapid Prototyp. J. 28 (2022) 1796–1807, https://doi.org/10.1108/RPJ-12-2021-0342.

[6] A. Ullah, K. Asami, K. Azher, C. Emmelmann, Comparative analysis of laser power, pure titanium, and titanium alloy effects on dendrite growth and surface morphology of TiO2-ceramic, J. Laser Appl. 36 (2024) 042061, https://doi.org/10.2351/7.0001601.

[7] A. Ullah, M. Shah, Z. Ali, K. Asami, A. Ur Rehman, C. Emmelmann, Additive manufacturing of ceramics via the laser powder bed fusion process, Int. J. Appl. Ceram. Technol. 22 (2025) e15087, https://doi.org/10.1111/ijac.15087.

[8] A.R. Bakhtari, H.K. Sezer, O.E. Canyurt, O. Eren, M. Shah, S. Marimuthu, A Review on Laser Beam Shaping Application in Laser-Powder Bed Fusion, Adv. Eng. Mater. 26 (2024) 2302013, https://doi.org/10.1002/adem.202302013.

[9] S. Chowdhury, N. Yadaiah, C. Prakash, S. Ramakrishna, S. Dixit, L.R. Gupta, D. Buddhi, Laser powder bed fusion: a state-of-the-art review of the technology, materials, properties & defects, and numerical modelling, J. Mater. Res. Technol. 20 (2022) 2109–2172, https://doi.org/10.1016/J.JMRT.2022.07.121.

[10] C. Qian, K. Zhang, J. Zhu, Y. Liu, Y. Liu, J. Liu, J. Liu, Y. Yang, H. Wang, Effect of processing parameters on the defects, microstructure, and property evaluation of Ti-6Al-4V titanium alloy processed by laser powder bed fusion, AIP Adv. 14 (2024) 025246, https://doi.org/10.1063/7.0001251.

[11] R. Haribaskar, T.S. Kumar, Defects in Metal Additive Manufacturing: Formation, Process Parameters, Postprocessing, Challenges, Economic Aspects, and Future Research Directions, 3D Print. Addit. Manuf. 11 (2024) e1629–e1655, https://doi.org/10.1089/3dp.2022.0344.

[12] T.M. Wischeropp, Hussein Tarhini, Claus Emmelmann, Influence of laser beam profile on the selective laser melting process of AlSi10Mg, 022059, J. Laser Appl. 32 (2) (May 2020) 1, https://doi.org/10.2351/7.0000100.

[13] J. Bi, L. Wu, S. Li, Z. Yang, X. Jia, M.D. Starostenkov, G. Dong, Beam shaping technology and its application in metal laser additive manufacturing: A review, J. Mater. Res. Technol. 26 (2023) 4606–4628, https://doi.org/10.1016/j.jmrt.2023.08.037.

[14] P. Kohlwes, Prozessstabile additive Fertigung durch spritzerreduziertes Laserstrahlschmelzen. Light Engineering für die Praxis, Springer Vieweg, Berlin, Heidelberg, 2024, https://doi.org/10.1007/978-3-662-69082-6.

[15] A. Bauch, P. Kohlwes, I. Kelbassa, Laser powder bed fusion of pure copper using ring-shaped beam profiles, J. Laser Appl. 36 (2024) 042021, https://doi.org/10.2351/7.0001562.

[16] T. Stoll, R. Prudlik, M. Birg, K. Wudy, Influence of different beam shapes on melt pool geometry of single melt tracks on IN718, Progress. Addit. Manuf. (2024), https://doi.org/10.1007/s40964-024-00775-x.

[17] F. Nahr, D. Bartels, R. Rothfelder, M. Schmidt, Influence of Novel Beam Shapes on Laser-Based Processing of High-Strength Aluminium Alloys on the Basis of EN AW-5083 Single Weld Tracks, J. Manuf. Mater. Process. 7 (2023), https://doi.org/10.3390/jmmp7030093.

[18] T.M. Wischeropp, Advancement of Selective Laser Melting by Laser Beam Shaping, Springer Vieweg, Berlin, Heidelberg, 2021, https://doi.org/10.1007/978-3-662-64585-7.

[19] M. Bayat, A. Thanki, S. Mohanty, A. Witvrouw, S. Yang, J. Thorborg, N.S. Tiedje, J. H. Hattel, Keyhole-induced porosities in Laser-based Powder Bed Fusion (L-PBF) of Ti6Al4V: High-fidelity modelling and experimental validation, Addit. Manuf. 30 (2019) 100835, https://doi.org/10.1016/j.addma.2019.100835.

[20] J.D. Pérez-Ruiz, F. Galbusera, L. Caprio, B. Previtali, de, L.N.L. Lacalle, A. Lamikiz, A.G. Demir, Laser beam shaping facilitates tailoring the mechanical properties of IN718 during powder bed fusion, J. Mater. Process. Technol. 328 (2024) 118393, https://doi.org/10.1016/j.jmatprotec.2024.118393.

[21] M. Godec, N. Mirzabeigi, Č. Donik, D.A. Skobir Balantič, S. Malej, I. Paulin, B. Podgornik, J. Grünewald, T. Novotny, F. Bayer, F. Ruiz-Zepeda, K. Wudy, Influence of laser beam shape and post heat-treatment on the microstructure and mechanical properties of nickel-based alloy IN718 manufactured by laser powder bed fusion, J. Mater. Res. Technol. 37 (2025) 1970–1986, https://doi.org/10.1016/j.jmrt.2025.06.119.

[22] L. Chechik, K. Schwarzkopf, R. Rothfelder, J. Grünewald, M. Schmidt, Material dependent influence of ring/spot beam profiles in laser powder bed fusion, Addit. Manuf. Lett. 9 (2024) 100211, https://doi.org/10.1016/j.addlet.2024.100211.

[23] K. Wang, D. Xie, F. Lv, F. Liu, R. Liu, D. Liu, J. Zhao, Stability of molten pool and microstructure evolution of Ti-6Al-4 V during laser powder bed fusion with a flat-top beam, Addit. Manuf. 75 (2023) 103756, https://doi.org/10.1016/j.addma.2023.103756.

[24] K. Joshi, P. Promoppatum, S.S. Quek, S. Raghavan, N.S. Johan, S. Shukla, S. Samudrala, S. van der Veen, M.H. Jhon, Effect of porosity distribution on the strength and strain-to-failure of Laser-Powder Bed Fusion printed Ti–6Al–4V, Addit. Manuf. 75 (2023) 103738, https://doi.org/10.1016/j.addma.2023.103738.

[25] V.-D. Le, E. Pessard, F. Morel, S. Prigent, Fatigue behaviour of additively manufactured Ti-6Al-4V alloy: The role of defects on scatter and statistical size effect, Int. J. Fatigue 140 (2020) 105811, https://doi.org/10.1016/j.ijfatigue.2020.105811.

[26] G. Li, W. Chi, W. Wang, X. Liu, H. Tu, X. Long, High cycle fatigue behavior of additively manufactured Ti-6Al-4V alloy with HIP treatment at elevated temperatures, Int. J. Fatigue 184 (2024) 108287, https://doi.org/10.1016/j.ijfatigue.2024.108287.

[27] A. Gupta, C.J. Bennett, W. Sun, N. Neate, On the microstructural evolution and failure mechanism in laser powder bed fusioned Ti–6Al–4V during low cycle fatigue at room and elevated temperatures, J. Mater. Res. Technol. 21 (2022) 4299–4319, https://doi.org/10.1016/j.jmrt.2022.10.141.

[28] M.A. Buhairi, F.M. Foudzi, F.I. Jamhari, A.B. Sulong, N.A.M. Radzuan, N. Muhamad, I.F. Mohamed, A.H. Azman, W.S.W. Harun, M.S.H. Al-Furjan, Review on volumetric energy density: influence on morphology and mechanical properties of Ti6Al4V manufactured via laser powder bed fusion, Progress. Addit. Manuf. 8 (2023) 265–283, https://doi.org/10.1007/s40964-022-00328-0.

[29] P. Ferro, R. Meneghello, G. Savio, F. Berto, A modified volumetric energy density–based approach for porosity assessment in additive manufacturing process design, Int. J. Adv. Manuf. Technol. 110 (2020) 1911–1921, https://doi.org/10.1007/s00170-020-05949-9.

[30] J. Grünewald, K. Wudy, Dimensionless process windows in laser-based powder bed fusion of AISI 316L using ring-shaped beam profiles, Addit. Manuf. Lett. 14 (2025) 100284, https://doi.org/10.1016/j.addlet.2025.100284.

[31] C. Smith, G. Hommer, M. Keeler, J. Gockel, K. Findley, C. Brice, A. Clarke, J. Klemm-Toole, Assessing Volumetric Energy Density as a Predictor of Defects in Laser Powder Bed Fusion 316L Stainless Steel, JOM 77 (2025) 737–748, https://doi.org/10.1007/s11837-024-06946-z.

[32] A. Ullah, A.E. Medvedev, D. Herzog, A. Molotnikov, T. Liu, I. Kelbassa, M. Brandt, Role of Laser Beam Shape and Energy Density in Modulating Surface Quality, Porosity, Microstructure, and Mechanical Properties of PBF-LB/M Ti-6Al-4V, J. Mater. Process. Technol. (2026) 119197, https://doi.org/10.1016/j.jmatprotec.2026.119197.

[33] A. Ullah, A.R. Bakhtari, A.E. Medvedev, A. Molotnikov, D. Herzog, I. Kelbassa, C. Emmelmann, M. Brandt, Effects of laser beam shaping on Ti-6Al-4V single tracks in PBF-LB/M: A study with Aconity MIDI+, Opt. Laser Technol. 192 (2025) 113762 https://doi.org/10.1016/j.optlastec.2025.113762.

[34] B. Meier, F. Warchomicka, J. Petrusa, R. Kaindl, W. Waldhauser, C. Sommitsch, High Temperature Tensile Strength of TI6AL4V Processed by L-PBF—Influence of Microstructure and Heat Treatment, BHM Berg- und Hüttenmännische Monatshefte 168 (2023) 247–253, https://doi.org/10.1007/s00501-023-01346-3.

[35] S.W.A. Shah, S. Ali, H. Ullah, M. Saad, A. Mubashar, E. Ud Din, Material characterization of Ti6Al4V alloy additively manufactured using selective laser melting technique, J. Mater. Res. Technol. 33 (2024) 1756–1763, https://doi.org/10.1016/j.jmrt.2024.09.164.

[36] T. Moloi, T.C. Dzogbewu, M. Maringa, A. Muiruri, Quasi-static tensile properties of DMLS TI6AL4V(ELI) specimens exposed to two different heat treatment processes and tested at different elevated temperatures, Results Eng. 22 (2024) 102290, https://doi.org/10.1016/j.rineng.2024.102290.

[37] S. Bergmueller, L. Gerhold, L. Fuchs, L. Kaserer, G. Leichtfried, Systematic approach to process parameter optimization for laser powder bed fusion of low-alloy steel based on melting modes, Int. J. Adv. Manuf. Technol. 126 (2023) 4385–4398, https://doi.org/10.1007/s00170-023-11377-2.

[38] Z. Li, C. Affolter, High-cycle fatigue performance of laser powder bed fusion Ti-6Al-4V alloy with inherent internal defects: A critical literature review, Metals 14 (2024) 972, https://doi.org/10.3390/met14090972.

[39] H. Sun, E.P. Busso, C. Ling, D.-F. Li, Crystal plasticity based investigation of the effects of additive manufactured voids on the strain localisation behaviour of Ti-6Al-4V, Int. J. Plast. 183 (2024) 104141, https://doi.org/10.1016/j.ijplas.2024.104141.

[40] J. Liu, K. Wang, R. Wang, Z. Yin, X. Zhou, A. Xu, X. Zhang, Y. Li, R. Wang, S. Zhang, J. Cheng, W. Bian, J. Li, Z. Ren, M. Sun, Y. Yang, D. Wang, J. Ren, Effect of lattice type on biomechanical and osseointegration properties of 3D-printed porous Ti6Al4V scaffolds, Int. J. Bioprint. 10 (2024) 1698, https://doi.org/10.36922/ijb.1698.

[41] C. Sithole, E.S. Abdelhady, A. Jalalian, S. Hoekstra, I. Gibson, Are density cubes sufficient to measure process performance and quality of geometrically complex parts in laser powder bed fusion? Int. J. Adv. Manuf. Technol. 139 (2025) 4211–4231, https://doi.org/10.1007/s00170-025-16146-x.

[42] G. Chen, C. Ren, X. Qin, J. Li, Temperature dependent work hardening in Ti–6Al–4V alloy over large temperature and strain rate ranges: Experiments and constitutive modeling, Mater. Des. 83 (2015) 598–610, https://doi.org/10.1016/j.matdes.2015.06.048.

[43] S. Ivanov, M. Gushchina, A. Artinov, M. Khomutov, E. Zemlyakov, Effect of elevated temperatures on the mechanical properties of a direct laser deposited Ti-6Al-4V, Materials 14 (2021) 6432, https://doi.org/10.3390/ma14216432.

[44] L. Afroz, S.B. Inverarity, M. Qian, M. Easton, R. Das, Analysing the effect of defects on stress concentration and fatigue life of L-PBF AlSi10Mg alloy using finite element modelling, Progress. Addit. Manuf. 9 (2024) 341–359, https://doi.org/10.1007/s40964-023-00457-0.

[45] V. Tvergaard, Material failure by void growth to coalescence, in: J.W. Hutchinson, T.Y. Wu (Eds.), Advances in Applied Mechanics, 27, Academic Press, San Diego, 1990, pp. 83–151, https://doi.org/10.1016/S0065-2156(08)70195-9.

[46] F. Wang, M. Li, Y. Zhang, F. Jiang, Y. Tong, M. Zarinejad, Laser directed energy deposition of NiTi shape memory alloys with herringbone grain architectures for enhanced ductility and superelasticity, Mater. Des. 261 (2026) 115355, https://doi.org/10.1016/j.matdes.2025.115355.

[47] Z. Li, J. Gou, J. Gao, J. Zhu, W. Kou, J. Wang, Microstructural evolution and corrosion resistance of additively manufactured Ti–6Al–4V alloy annular shaped components using multistage heat treatment, Mater. Chem. Phys. 346 (2025) 131414, https://doi.org/10.1016/j.matchemphys.2025.131414.

[48] A.K. Dwivedi, I.A. Khan, J. Chattopadhyay, On the role of shape and distribution of secondary voids in the mechanism of coalescence, Eng. Fract. Mech. 289 (2023) 109399, https://doi.org/10.1016/j.engfracmech.2023.109399.

[49] Z. Men, L. Wang, X. Gao, W. Chen, C. Ji, Z. Li, K. Li, Accurate Detection and Analysis of Pore Defects in Laser Powder Bed Fusion WE43 Magnesium Alloys, Micro (Basel) 15 (2024), https://doi.org/10.3390/mi15070909.